USING DEPOLARIZATION TO QUANTIFY ICE NUCLEATING PARTICLE CONCENTRATIONS: A NEW METHOD

A Thesis

by

JOHN PAUL ZENKER III

Submitted to the Office of Graduate and Professional Studies of
Texas A&M University
in partial fulfillment of the requirements for the degree of

MASTERS OF SCIENCE

Chair of Committee,	Sarah D. Brooks
Committee Members,	Renyi Zhang
	Qi Ying
Head of Department,	Ping Yang

August 2017

Major Subject: Atmospheric Sciences

ABSTRACT

We have developed a new method to determine ice nucleating particle (INP) concentrations observed by a Continuous Flow Diffusion Chamber (CFDC) under a wide range of operating conditions. In this study, we manipulate differences in particle optical properties detected by the Cloud and Aerosol Spectrometer with POLarization (CASPOL) to differentiate ice crystals, droplets, and aerosols. The depolarization signal from the CASPOL instrument is used to determine the occurrence of water droplet breakthrough (WDBT) conditions in the CFDC, under which the traditional analysis method fails. To overcome the challenge of WDBT, we design a new analysis method using depolarization ratio that can extend the range of operating conditions of the CFDC. The method agrees reasonably well with the traditional method under non-WDBT conditions with a mean percent error of ± 32.1 %. Additionally, a comparison with the Colorado State University (CSU) CFDC is used to show that the new analysis method can be used reliably during WDBT conditions. Due to the high detection limit of the CASPOL, the new method is only suitable for laboratory use when high INP concentrations (> 50,000 L^{-1}.) can be generated and not for ambient measurements where the INP concentration is ≤ 100 L^{-1}.

DEDICATION

To the countless number of people who have loved and supported me through the journey of grad school, especially Sean Chalk for his patience, understanding and encouragement when I needed it the most.

To all of the teachers and mentors that have inspired my thirst for knowledge that will never be quenched.

ACKNOWLEDGEMENTS

I would like to thank my advisor Dr. Sarah Brooks for her commitment to my growth as a scientist and researcher. This achievement would not be possible without her investment in time and effort to this project.

CONTRIBUTORS AND FUNDING SOURCES

Contributors

This work was supervised by a thesis committee consisting of Dr. Sarah Brooks and Dr. Renyi Zhang of the Department of Atmospheric Sciences and Dr. Qi Ying of the Department of Civil Engineering.

The modeling calculations in section 3.2 analyses were conducted in part by Guanglang Xu of the Department of Atmospheric Science under the guidance of Dr. Ping Yang. Data from the Colorado State University in section 3.8 was provided by Dr. Paul DeMott with the assistance of Ezra Levin and Kaitlyn Suski.

All other work conducted for the thesis was completed by the student independently.

Funding Source

This work was funded by the NSF Environmental Chemistry: Grant # 1309854.

TABLE OF CONTENTS

Page

LIST OF FIGURES

Page

LIST OF TABLES

Page

1. INTRODUCTION

Ice clouds cover approximately 40% of the earth's atmosphere and present a challenge in the understanding of our global radiative budget (Wylie and Menzel, 1999). Because of their complicated microphysical properties, high altitudes in the atmosphere, and optically thin features, these clouds pose a pronounced challenge in the understanding of our global radiative budget (Wendisch et al., 2005, Zhang et al., 1999, Yang et al., 2015). Despite a significant amount of effort of the atmospheric research community in the last several decades to study ice clouds, there are still large gaps in our understanding of the impact they have on our climate (Boucher et al., 2013).

Ice crystals can nucleate via several mechanisms (Vali et al., 2015, Vali, 1985). At temperatures below -36^{o}C, ice crystals begin to nucleate homogenously from water droplets. At higher temperatures, an ice nucleating particle (INP) is needed to facilitate the formation of an ice crystal via heterogeneous nucleation. An aerosol can induce depositional freezing, which was originally envisioned as water vapor depositing directly to ice on the aerosol surface. However, recent work suggests that the exact mechanism may first involve condensation of water in surface features prior to freezing (Marcolli, 2014). Alternatively, immersion freezing may occur, when an aerosol becomes embedded within a water droplet thereby causing the droplet to freeze. Condensational freezing can also occur when a soluble aerosol acts as a cloud condensation nuclei (CCN) in a warm environment to form a droplet, which later enters a cooler environment

and nucleates an ice crystal. However, the distinction between this mechanism and immersion freezing is unclear. Evidence suggests that immersion freezing owes the largest contribution to ice crystal nucleation in clouds (De Boer et al., 2011, Murray et al., 2012). Finally, a third heterogeneous mechanism is contact freezing during which an aerosol comes in contact with a water droplet surface and freezes. While the exact mechanism of contact freezing remains unresolved, it has been shown that the presence of an INP positioned at a droplet surface facilitates the freezing process at temperatures several degrees warmer than immersion freezing on identical INP (Fornea et al., 2009, Durant and Shaw, 2005). Information about the action of these mechanisms for formation of ice in mixed-phase clouds (containing droplets and ice crystals) may be particularly important for developing robust parameterizations for global climate model (GCMs).

Composition, surface structure, and size are important factors in determining the ice nucleating ability of an aerosol (Zolles et al., 2015, Niemand et al., 2012). Field measurements suggest that K-feldspar, a common component of soil dust aerosol, may account for a large fraction of Earth's INPs (Atkinson et al., 2013, Yakobi-Hancock et al., 2013). Recent investigations of other aerosols have identified secondary organic aerosols (SOA), other marine aerosols, and aerosols produced from biomass burning as effective INPs (DeMott et al., 2016, McCluskey et al., 2016, Levin et al., 2016, McCluskey et al., 2014, Collier and Brooks, 2016).

Optical techniques have been used to detect and characterize ambient ice crystals (Mishchenko and Sassen, 1998, Yoshida et al., 2010, Noel and Sassen, 2005). For

example, lidar observations can use the depolarization ratio to distinguish cloud particle type (i.e., ice crystals or water droplets). In traditional lidar applications, the depolarization ratio is calculated using Eq. (1),

$$\delta_{LIDAR} = \frac{B_{\perp}}{B_{\parallel}} \quad (1)$$

where $B_{\perp}$ and $B_{\parallel}$ are the perpendicular and parallel components of the retrieved lidar signal from the ambient atmosphere or clouds. Under single scattering condition, the depolarization ratio associated with an ensemble of water droplets is essentially zero while the counterpart for ice crystals is nonzero with a specific value depending on particle habit and orientation. Ice crystal depolarization ability is attributed to the high irregularities in the shapes and surfaces of ice crystals.

The number of INPs present in a cloud can dictate its optical properties throughout the ice nucleation process (Hoose and Möhler, 2012, Murray et al., 2012). Chambers that reproduce ice nucleation conditions have been used for the last 30 years to take INP measurements. Techniques used to detect and measure nucleated ice crystals in these devices are still under development for several reasons. First, It is difficult to measure INP with ice chambers because the concentration of effective INP is typically 0.1 to 1000 L^{-1} or ~10^{-4} to 10^{-6} of the total aerosol concentration (DeMott et al., 2003, DeMott et al., 2015, Jiang et al., 2014, Mason et al., 2016). Secondly, differentiating between ice crystals and droplets that form in the chamber is essential and can be difficult to account for. The Continuous Flow Diffusion Chamber (CFDC) was originally developed by Rogers (1988) at the University of Wyoming and was later modified and rebuilt at Colorado State University (CSU). The CSU CFDC has been

operated in multiple field projects each year for the past 15 years (Creamean et al., 2013, DeMott et al., 2015, Prenni et al., 2013). Several other ice chambers have been developed since then including the CFDC at Texas A&M University (TAMU) that is used in this study. Many enhancements have been made to CFDCs (Rogers et al., 2001). An enhancement made to the TAMU CFDC is the replacement of a traditional aerosol spectrometer (CLIMET, Model No. CI-3100), which uses particle size to distinguish ice crystals from water droplets and aerosols, with the Cloud and Aerosol Spectrometer with POLarization (CASPOL). The CASPOL detects forward scattering, backward scattering and depolarization on a single particle basis. The instrument has previously been used to differentiate between ice crystals and various types of dust and soil particles (Glen and Brooks, 2014, Glen and Brooks, 2013).

Several previous studies have designed new analysis methods for ice chambers that utilize the depolarization ratio measured by an OPC that operate similarly to the CASPOL (Nicolet et al., 2010, Clauss et al., 2013, Garimella et al., 2016). Nicolet et al. (2010) accurately quantified ice crystals in the presence of water droplets in a chamber by using the peak intensity of the depolarization ratio to discriminate ice crystals with the Ice Optical DEtector (IODE). Rather than using the peak intensity of the depolarization signal to detect ice crystals, Clauss et al. (2013) used the width of the pulse detected in the depolarization channel of the TOPS-ice instrument to differentiate between ice crystals and water droplets. Alternatively, Garimella et al. (2016) used a machine learning technique with scattering signals, including linear depolarization signals, detected by an OPC installed in the SPectrometer for Ice Nuclei (SPIN, DMT,

Inc.) to detect INP. In this study, we demonstrate how differences in particle optical properties can be used to differentiate between ice crystals, droplets, and aerosols detected by the CASPOL. In addition, we designate a new method to quantify INP concentrations detected by the CFDC using depolarization ratio, and determine the accuracy of that method in comparison to the traditional analysis method that primarily uses particle size to identify activated ice crystals as INPs.

2. EXPERIMENTAL

The data presented here were collected during the second phase of the Fifth International Ice Nucleation Workshop campaign (FIN 02), which took place at the Institute of Meteorology and Climate Research: Atmospheric Aerosol Research (IMK-AAF) facility at the Karlsruhe Institute of Technology (KIT) in Karlsruhe, Germany. There are two specialized chambers at (KIT) that were used in this campaign: the Aerosols Interaction and Dynamics in the Atmosphere (AIDA) chamber and the Aerosol Preparation and Characterization (APC) chamber. The AIDA chamber can be used to simulate atmospheric conditions that give rise to cloud particle nucleation and growth, and has been used in many previous campaigns and instrument intercomparisons to examine the ice nucleating ability of various aerosols (Amato et al., 2015, Schnaiter et al., 2016, Wagner et al., 2015, DeMott et al., 2011). The AIDA chamber is a three-story, 84 m^3 volume that uses adiabatic expansion to simulate the atmospheric conditions required for ice nucleation to occur. The second chamber, the APC, is a 3.7 m^3 volume with controlled and homogenous conditions (Linke et al., 2006). It was used during FIN 02 to provide aerosol populations of additional compositions. During the FIN 02 campaign groups from 22 institutions sampled both chambers using a variety of online and offline ice nucleation measurement methods. For verification of our TAMU CFDC measurements and new analysis method, we will compare our results to the measurements of the CSU CFDC. In order to test the CASPOL detector response to ice

and non-ice particles, auxiliary measurements of olive oil droplets, ambient aerosols, and homogeneously frozen ice crystals are also evaluated and compared to the CFDC-CASPOL heterogeneous nucleation data collected during FIN 02.

2.1 The Continuous Flow Diffusion Chamber (CFDC)

The TAMU CFDC was custom built in our laboratory at Texas A&M University and has been operated in previous laboratory and field campaigns to take temperature and supersaturation resolved INP concentration measurements (Glen and Brooks, 2014, McFarquhar et al., 2011).

Sample aerosols pass through a diffusion dryer to remove moisture from the air and aerosols before they enter the CFDC. Typically, aerosols flow through an impactor, prior to entering the CFDC, in order to remove aerosols with a diameter greater than ~1.3 μm from the sample flow. However, no impactor was used during the FIN 02 campaign since aerosol size distributions were well characterized and were sufficiently small. The aerosols then enter the CFDC where temperature and supersaturation are controlled. The CFDC consists of two concentric cylindrical walls coated with ice. Separate refrigeration units on each wall can be controlled to create a temperature gradient in the chamber that imposes a region of supersaturation with respect to ice (SS_i) in the CFDC. The CFDC chamber is 39" long. The bottom 12” of the inner wall is coated with hydrophobic Teflon to prevent water from freezing to the wall in this region. This section of the chamber is referred to as the evaporation region because it remains subsaturated with respect to water and partially or completely evaporates water droplets

that nucleate in the CFDC. The separate wall temperatures are manually controlled and monitored through a Labview program. The temperature and supersaturation conditions at the position of the sheath-air surrounded aerosol lamina are calculated using analytical equations reported in Rogers (1988).

Before measurements can be taken with the CFDC, the chamber must be prepared. First, a vacuum pump is used to evacuate the chamber for approximately 30 minutes in order to eliminate ambient aerosols that may have infiltrated the chamber and to remove moisture that may cause the walls to accumulate an uneven coating of ice or allow ice to accumulate in other sensitive regions. The walls are then cooled to a temperature of -25 °C and the CFDC walls are iced by pumping Nanopure water into the chamber from the base. Excess water is drained out of the instrument for approximately a minute after icing is complete. Then, the chamber is evacuated and refilled with N_2 gas once more before sampling is initiated.

At the base of the processing chamber, particles pass to a detector to determine INP concentration. In previous TAMU CFDC studies, either an optical particle counter (Climet, Inc.) or the Cloud and Aerosol Spectrometer with Polarization (CASPOL) were employed.

2.2 The Cloud and Aerosol Spectrometer with POLarization (CASPOL)

The CASPOL is a prototype particle-by-particle counter used in previous studies to detect and distinguish between dust and ice particles and even between various types of dust (Glen et al., 2013, 2014). The CASPOL instrument has three detectors that give

information about the optical properties: A forward scatter detector, a backward scatter detector with a parallel polarized filter, and a backwards scatter detector with a perpendicular polarized filter. In addition, the instrument has a fourth detector that determines if a particle is properly aligned in the laser beam and should thus be recorded.

2.3 CFDC-CASPOL operating procedure and analysis

Once the CFDC has been prepared as specified in section 2.1, the CASPOL is installed at the base of the chamber. Then, two mass flow controllers are used to set the total flow and sheath flow through the chamber. The difference between the total and sheath flows imposes the sample flow. For this campaign, the total flow was set to values ranging from 6 to 9 L min^{-1} and the sheath flow was set to values ranging from 4 to 7 L min^{-1} resulting in a sample flow that was typically ~2 L min^{-1}. During operation, the CFDC made scans from low to high supersaturation at a set lamina temperature (± 1.5 °C). This is accomplished by increasing wall temperature difference in a manner that retains the desired temperature at the sample lamina position.

CFDC-CASPOL data is sorted into 1-minute segments in order to achieve a sufficient sample volume detected by the CASPOL. The temperature, pressure, and sample and sheath flows are used to determine a STP (standard temperature and pressure) sample volume, which is used to convert the raw count of particles in each 1-minute segment to a concentration. Occasionally ice particles may detach from ice-coated chamber walls. To account for this, before and/or after each supersaturation scan

was taken, a zero filter is placed ahead of the sample inlet in order to determine background signal of the CFDC chamber. This background is subtracted from the total concentration measured by the CFDC-CASPOL.

The traditional analysis method counts INPs based on a nominal size cut of 2 or 5 μm in diameter in order to discriminate between unactivated aerosols and ice crystals. The CASPOL signal is accurately calibrated for spherical particles. For non-spherical ice crystals, the particle size-scattering relationship is less certain. Thus, the 2 and 5 μm size cuts are only approximate.

2.4 Limitations of the traditional analysis method

There are several limitations to the traditional analysis method used to process CFDC data (as described in Section 2.4). As previously mentioned, in supersaturated conditions with respect to water (SS_w), supercooled water droplets form in the chamber. At high supersaturations, water droplets may pass through the evaporation region without fully evaporating. Particles that remain larger than the 2 μm size cut will be miscounted as ice crystals. This phenomenon is referred to as water droplet breakthrough (WDBT). WDBT is an issue intrinsic to continuous flow ice nucleation instruments, although the point at which WDBT occurs varies between instruments of differing dimensions and even as a function of operating conditions (especially temperature) within a single instrument (DeMott et al., 2015). Furthermore, in some cases, it can be difficult to discern when WDBT is occurring with the current analysis method, so there is an opportunity for positive and negative artifacts. Generally, WDBT arises due to the

operating conditions of the CFDC set by the user, but WDBT could be exacerbated if the aerosol entering the chamber is not sufficiently dried under moist ambient conditions. A new analysis method is needed to overcome the challenges presented by WDBT (Rogers et al., 2001).

For the traditional analysis method to be successful sample aerosols must not be larger than the applied size cut or they too will be miscounted as an INP. To avoid miscounting aerosols as INP, a BGI Sharp Cut Cyclone (SCC) Model 0.732 is typically installed during ambient measurements, as mentioned above, to prevent any particles larger than ~ 1.3 μm from entering the CFDC. However, depending on the sample flow of the CFDC ~1 to 10% of particles larger than 2 μm may still make it through the impactor and into the chamber to contribute to the apparent INP signal. A new analysis method that allows for the inclusion of larger aerosols could improve our measurements of INPs, especially at low SS_w and higher supercooled temperatures.

2.5 CASPOL depolarization ratio definition

The goal of this study is to design an improved analysis method that uses single-particle depolarization ratio to identify ice crystals in order to quantify INP. In this study, the depolarization ratio is defined as follows (Glen et al., 2014).

$$\delta_{CAS} = \frac{B_{\perp,CAS}}{B_{\perp,CAS} + B_{\parallel,CAS}} \quad (2)$$

This definition differs somewhat from the conventional depolarization ratio used in remote sensing based on lidar observations. The main difference is that the CASPOL detects light at the back scattering angles of 168° to 176°, rather than precisely 180° in

the case of lidar. Secondly, the CASPOL occasionally detects a particle for which the parallel backscatter signal is below the limit of detection and thus is registered as zero, while the same particle has a nonzero perpendicular signal. In such cases, the calculated lidar depolarization ratio of such particles is infinite. In contrast, the value of depolarization ratio calculated by Eq. (2) is 1 making the depolarization ratio of these particles quantitatively meaningful.

2.6 Auxiliary CASPOL measurements

In order to develop the new analysis method, particle measurements were taken with the CASPOL independent of the CFDC to provide instrument response to various types of particles, which may coincidently reach the detector during CFDC-CASPOL operation.

One population of interest is water droplets. Using a Vibrating Orifice Aerosol Generator (VOAG) (TSI, Inc., Model 3450) with olive oil solutions is a standard method used to produce monodisperse spherical droplets of chosen sizes. Though the index of refraction of olive oil (1.44 to 1.47) is slightly higher than water (1.33), these droplets are a suitable approximation for the depolarization ratio signal of water droplets because they are uniform spheres. For this project 2, 6, 8 and 10 μm droplets were generated. A separate olive oil and 2-propanol solution is prepared for each desired size and the vibration frequency, and dispersion and dilution flows are set according to computed specifications as detailed in the VOAG manual and as previously performed in Glen (2014b).

During VOAG-CASPOL sampling, the olive oil aerosol stream first travels through a neutralizer to prevent particle loss. Following the neutralizer, a dump line allows for excess flow generated from the VOAG to be expelled from the sample line. The sample that travels to the CASPOL is controlled by a mass flow controller and a Gast air pump on the downstream side. Aerosols are sampled for roughly 15 minutes during which approximately 10,000 droplets are sampled. Small residual droplets of 2-propanol that do not evaporate remain in the sample flow and are detected by the CASPOL. For this reason, all particles less than 1 μm are removed from the dataset during processing.

A second population of interest is ambient aerosol. Aerosol was sampled at the Storm Peak Laboratory (SPL) in Steamboat Springs, CO in September 2015 for ninety-two hours over a seven day period. The use of a diverse aerosol population is necessary to ensure that the new analysis method be successful at discriminating ice crystals in the CFDC from a wide range in aerosols. SPL is an ideal sampling location because the aerosol population comes from many sources including mineral dust, organics from deciduous and coniferous forests, biomass burning aerosols that have been transported from forest fires in the western United States, and sulfates that are produced by two coal burning power plants that are both approximately 50 km and 100 km from the laboratory.

Ambient aerosol sampling at SPL was accomplished by connecting the CASPOL directly to an ambient sample inlet in the laboratory. Thirdly, CFDC measurements were taken under homogenous freezing conditions to generate ice crystals (Glen et al., 2014).

For these measurements, the sample flow was conditioned with a pre-cooler, which was set at -10 ^{o}C to remove excess moisture and the CFDC was operated at 51 % ± 2.3 % SS_i (supersaturation with respect to ice), -27 % ± 1.5 % SS_w and at –55 ^{o}C ± 0.2 ^{o}C. Under the flow and SS conditions at these low temperatures, only a fraction of homogeneously frozen particles will exceed 2 microns diameter. For this reason, all particles less than 2 microns are removed from the dataset. We can safely assume that all particles larger than this size were frozen, which is the goal of this experiment.

For clarity, the VOAG droplets, ambient aerosols collected at SPL, and ice crystals generated in homogenous conditions will be referred to as droplet, aerosol, and ice crystal training datasets respectively.

3. RESULTS

3.1 Discriminating water droplets, aerosols, and ice crystals with optical signatures

This analysis used optical differences between ice crystals, droplets, and aerosols in order to identify and quantify ice crystals that form in the CFDC. The CASPOL has been used previously to discriminate between different aerosol populations using an empirical tool known as an optical signature (Glen et al., 2013). In an analogous method, optical signatures produced from CALIPSO satellite data of various types of clouds have been reported by Hu et al. (2009).

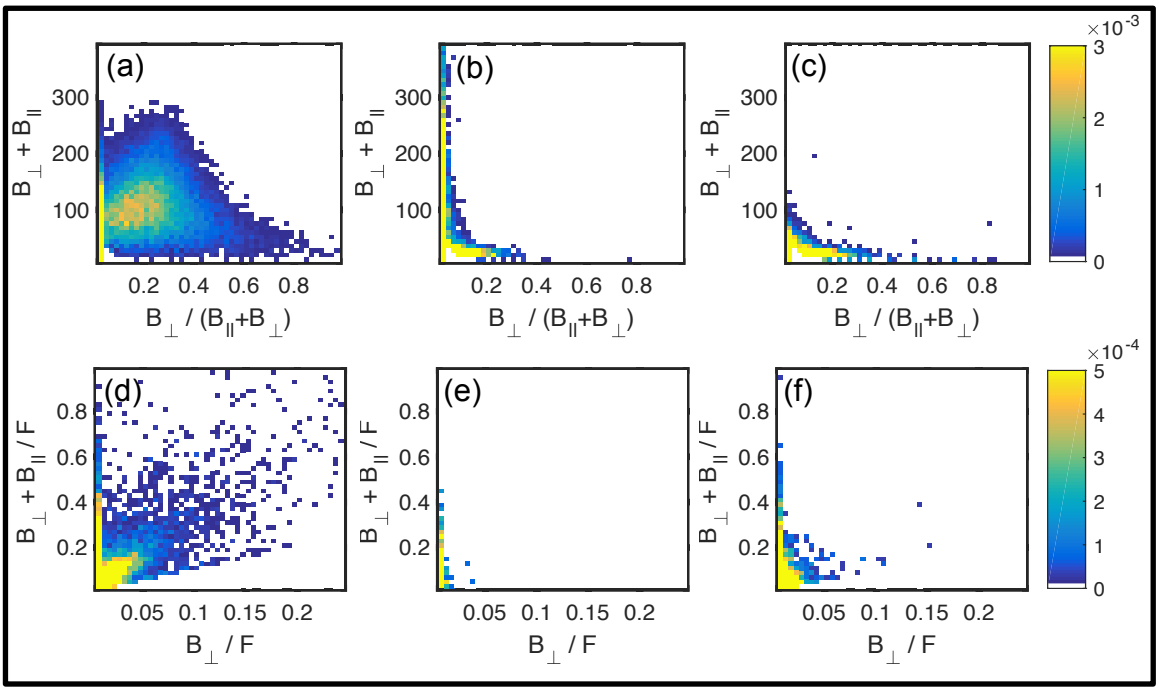

Figure 1. Optical signatures of training data populations: ice crystals (a, d), droplets (b, e), and aerosol (c, f). The CASPOL signals used to generate these signatures are parallel back scatter ($B_{||}$), perpendicular back scatter ($B_{\perp}$), and forward scatter (F). The shading scales indicate the fraction of the training dataset that populates a grid cell.

Optical signatures for the training datasets are displayed in Figure 1. Optical signatures for ice training, droplet and aerosol training data are shown in 1a-c, respectively. These signatures show depolarization ratio (as defined in Eq. (2)) versus total backscatter. The optical signatures are generated by defining a 50 x 50 Cartesian grid with depolarization ratio on the x-axis and total backscatter (calculated as the sum of the CASPOL's parallel and perpendicular signal intensities) on the y-axis. Each particle detected by the CASPOL is placed in the appropriate grid cell. The color scale displays the fraction of particles in a dataset that populate that grid cell. As discussed,

the ice crystal and droplet training data shown in Figure 1 only includes particles with $D_p \geq 2$ μm and $D_p \geq 1$ μm respectively. Each training dataset contains particles that are exclusively highly backscattering (> 75) or highly depolarizing (> 0.1), but only the ice crystal population contains particles that have both a high depolarization ratio and high backscatter signal. In Figures 1 d-f, normalized optical signatures with respect to forward scatter, F, are displayed. Here the total backscatter signal to forward scatter signal ratio is plotted against the back perpendicular signal to forward signal ratio. The back perpendicular to forward ratio is a measure of depolarizing ability normalized by size (which is determined by the forward signal, F). In Figures 1 d-f, we see that very few aerosols and droplets achieve a back perpendicular to forward ratio > 0.05. In contrast, many of the ice crystal training dataset particles exceed that value.

Consistent with the findings of Glen et al (2013), CASPOL optical signatures can be used as an empirical tool to detect differences in the bulk optical properties of different particle populations. However, in order to design a new analysis method, it is necessary to gain a quantitative understanding of how the CASPOL detects single-particles as opposed to bulk populations of particles.

3.2 Modeling the depolarization ratio of water droplets, aerosols, and ice crystals

Model calculations can provide insight as to how particles depolarize light in the CFDC. In order to generate model calculations, we first must define the relation between the CASPOL depolarization ratio (Eq. 2) and the scattering phase matrix. It is assumed

that the CASPOL emits an incident beam that propagates along the z direction in the form

$$\boldsymbol{E}_i = \begin{pmatrix} E_{\parallel i} \\ E_{\perp i} \end{pmatrix} e^{ik(r-z)} = \begin{pmatrix} E_{\parallel i} \\ 0 \end{pmatrix} e^{ik(r-z)} \tag{3}$$

where $\mathbf{E_i}$ is the incident electric field, $E_{\parallel i}$ and $E_{\perp i}$ (=0) are the parallel and perpendicular components with respect to the scattering plane, k is wavenumber, ω is frequency, and t is time. The scattering plane is defined as a plane though the z-axis and the line linking the particle and detection point. The scattered light at a sufficiently large distance (i.e., in the far-field zone) is related to the incident light in the form

$$\boldsymbol{E}_s = \frac{e^{ik(r-z)}}{-ikr} \begin{pmatrix} S_2 & S_3 \\ S_4 & S_1 \end{pmatrix} \begin{pmatrix} E_{\parallel i} \\ 0 \end{pmatrix} = \frac{e^{ik(r-z)}}{-ikr} \begin{pmatrix} S_2 \\ S_4 \end{pmatrix} E_{\parallel i} \tag{4}$$

where r is the distance between the particle and detector, and S_{ij} is the amplitude matrix. The model depolarization ratio δ_{Model} can be expressed as follows.

$$\delta_{Model}(\theta) = \frac{B_{\perp,Model}(\theta)}{B_{\perp,Model}(\theta) + B_{\parallel,Model}(\theta)} = \frac{|S_4(\theta)|^2}{|S_4(\theta)|^2 + |S_2(\theta)|^2} \tag{5}$$

where θ is the detection angle, and $B_{||,Model}$ and $B_{\perp,Model}$ are the modeled parallel and perpendicular backscattered intensities. Using the following relations between the scattering phase matrix, P_{ij} the amplitude matrix S_{ij} and the scattering cross section C_{sca} below,

$$|S_4(\theta)|^2 + |S_2(\theta)|^2 = (P_{11}(\theta) + P_{12}(\theta)) \times C_{sca} \tag{6}$$

$$|S_4(\theta)|^2 - |S_2(\theta)|^2 = (P_{21}(\theta) + P_{22}(\theta)) \times C_{sca} \tag{7}$$

we can define the depolarization ratio from the CASPOL that is analogous to the mean modeled depolarization ratio over the angular range of 168° to 176° and is expressed below in (8).

$$\bar{\delta}_{Model}(168°:176°) = \frac{\int_{168°}^{176°}(P_{11}(\theta) + P_{12}(\theta) - P_{21}(\theta) - P_{22}(\theta))\ \sin(\theta)\, d\theta}{2\int_{168°}^{176°}(P_{11}(\theta) + P_{12}(\theta))\ \sin(\theta)\, d\theta} \quad (8)$$

We apply an improved geometric optics method (IGOM) and a T-matrix method to compute the scattering phase matrices of the ice crystals and dust-like particles, respectively (Yang and Liou, 1996, Bi et al., 2013, Liu et al., 2013). The T-Matrix method provides a more accurate calculation, but due to the large size of ice crystals, the method is not used due to the computational expense.

Three idealized ice crystal habits were modeled: a hexagonal column, a hexagonal plate, and a droxtal. These shapes represent generalizations of common ice crystal habits (Bailey and Hallett, 2009). An idealized dust-like particle with fractal facets was used to model aerosols (Liu et al., 2013). These particles are irregularly shaped and thus will yield different measured depolarization ratios depending on their orientation in the CASPOL. The model provides the mean depolarization ratio over all orientations. In contrast, the theoretical depolarization of water droplets is zero at all sizes.

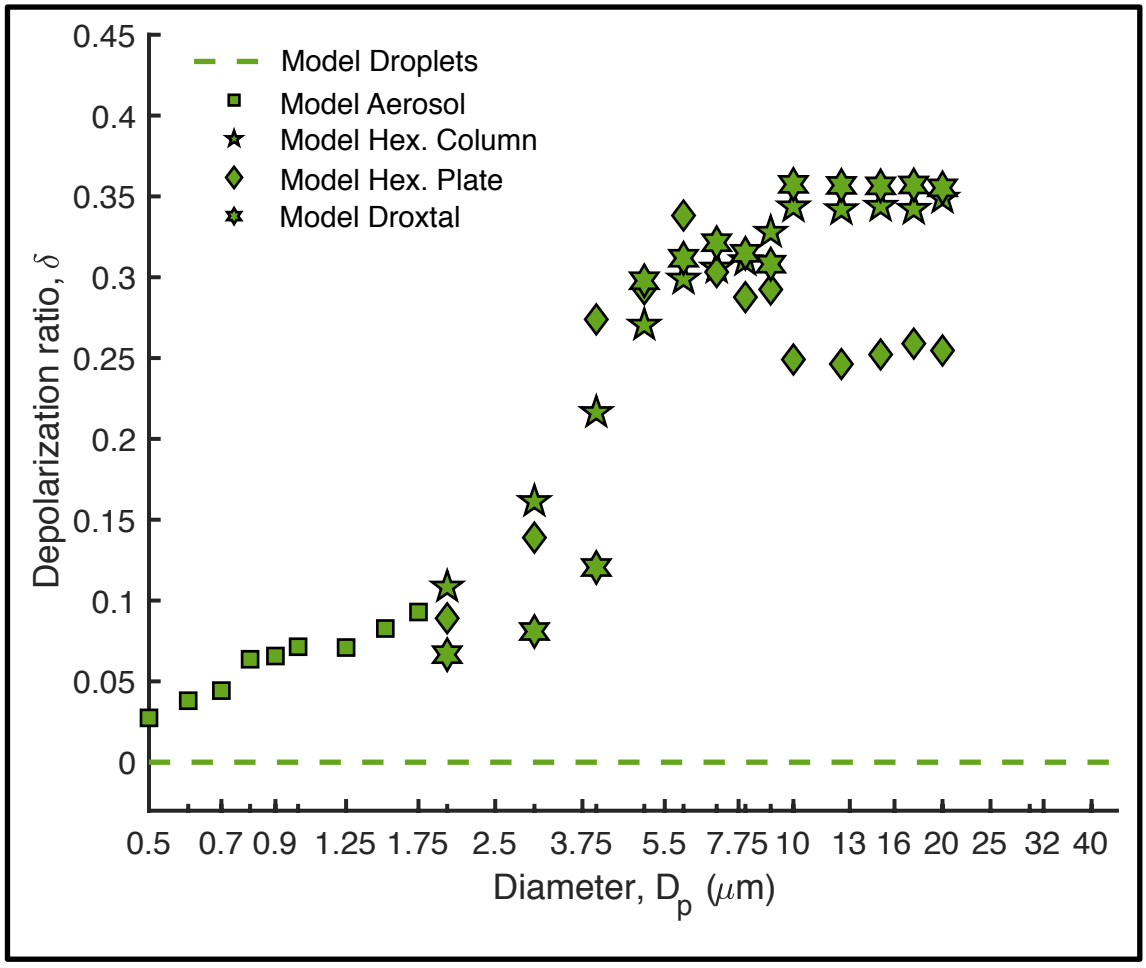

Figure 2. Depolarization ratio vs. diameter for modeled particles: droplets (dashed line), aerosols (square), hexagonal column ice crystals (pentagram), hexagonal plate ice crystals (diamond), and droxtals (hexagram).

Figure 2 shows the depolarization ratios vs. size for the three ice crystal habits, dust-like aerosol, and water droplets. We notice that ice crystals have a relatively high depolarization ratio in comparison to aerosols and water droplets, which confirms and expands on the bulk population observations from optical signatures in Figure 1. The

calculations performed in this section provide confidence that ice crystals can be distinguished from aerosols and water droplets in the CFDC under all expected conditions using depolarization ratio.

3.3 Determination of optical properties of aerosols, droplets, and ice crystals

In this section, we test the assertion that the CASPOL depolarization ratio can be used to discriminate ice crystals from aerosols and water droplets. To accomplish this, the training datasets of droplets, aerosols, and ice crystals in Figure 1 are examined further. The lognormal size distributions (shown as a percent of population) observed by the CASPOL for the droplet, aerosol, and ice crystal training data are shown in Figure 3a. Each nominal VOAG size in the droplet training dataset is plotted as a separate line. The size distributions of droplets, aerosols and ice crystals overlap. This demonstrates the primary disadvantage to using particle diameter as the sole criteria to identify ice crystals.

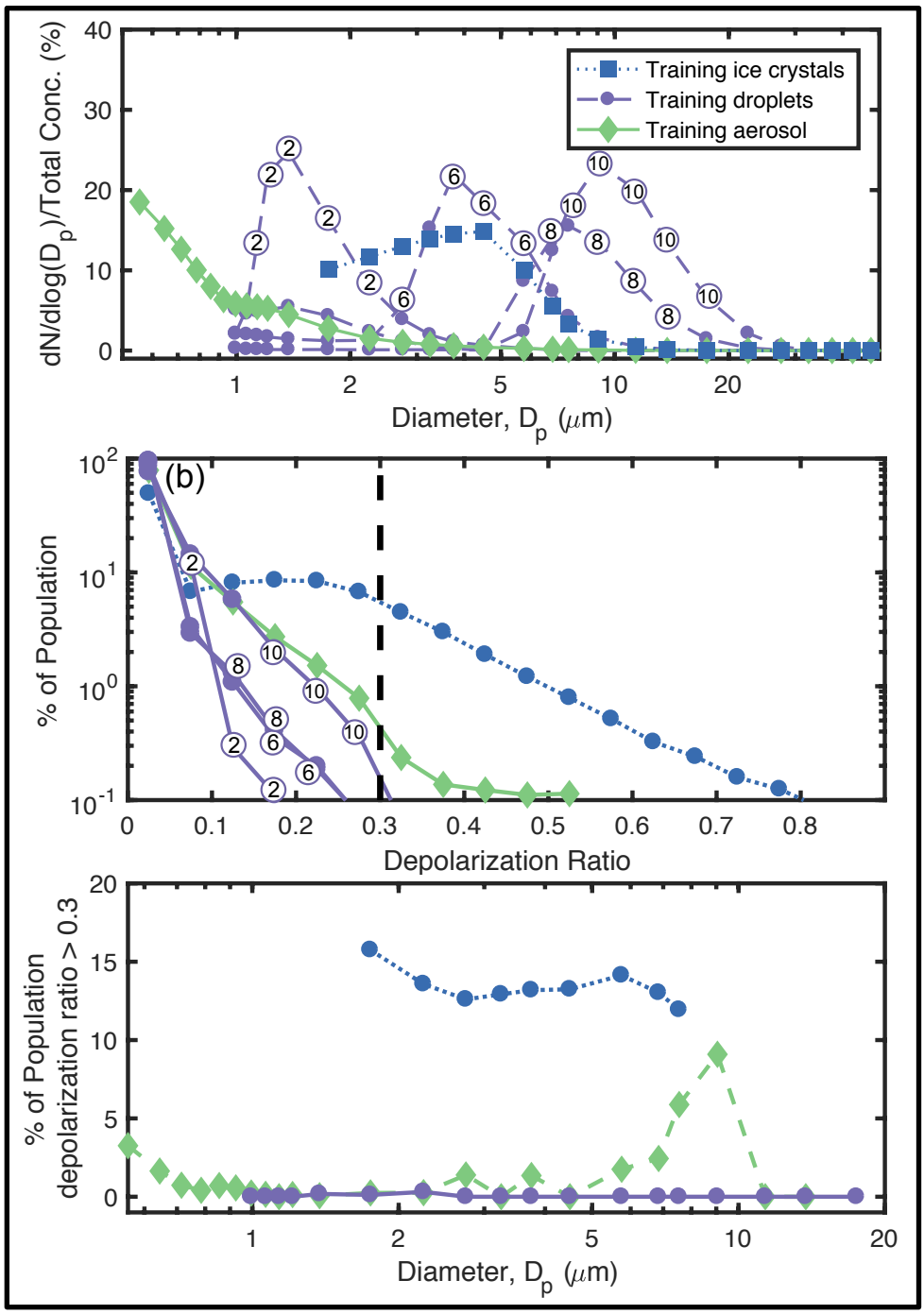

Figure 3. (a) Percent lognormal size distribution, (b) depolarization ratio distributions, and (c) the percentage of the particles with depolarization ratios above the threshold of 0.3 are shown for training data droplets, aerosols, ice crystals. In 1b, the depolarization ratio threshold value of 0.3 is indicated by the dashed line. In Figures a and b, the numbers displayed in circles provide the diameter in μm of the VOAG data represented by that line.

The normalized depolarization ratio distributions for the 3 training datasets are shown in Figure 3b. In Figure 3c, the percent of particles that achieve a depolarization ratio ≥ 0.3 (the nominal selection criteria for depolarizing ice crystals) as a function of particle diameter is shown. In Figure 3c, the droplet training data collected for all sizes of olive oil droplets is combined and displayed as one line for simplicity. In contrast to the size distributions (Figure 3a), in which the training datasets cannot be discriminated, the depolarization ratio distributions show notable differences between droplets, aerosols, and ice crystals. Figure 3b and c reveal that only 0.3% of droplets and 1.6% of aerosols achieve a depolarization ratio ≥ 0.3. The exception to this is aerosols with diameters of 5 to 10 μm. In this size range, 3.9 % percent of aerosols achieve a depolarization ratio of 0.3. However, 5 to 10 μm particles are not abundant in nature, cannot easily be sampled by real-time instruments having the inlet complexity of a CFDC, and only represent 0.3% of the aerosol training dataset. Furthermore, particles in this size range were not generated during the FIN 02 campaign. In contrast, 13.5 % of particles in the ice crystal training dataset achieve a depolarization ratio of at least 0.3. This natural break in the depolarization ratio distributions can be considered as a threshold for which particles above the threshold are ice. Below the threshold, the identity of particles is unknown since the majority of all three populations have depolarization ratios between 0 and 0.3.

3.4 Determining WDBT conditions in CFDC runs

As discussed in section 2.5, WDBT can be difficult to identify when relying on the traditional analysis method. To better determine periods when WDBT conditions are occurring in the CFDC, particle size distributions and depolarization can be considered. In this manuscript, the onset of water droplet breakthrough is analytically defined as the time period where a continuous size distribution extends from the small size bins past the 2 μm threshold. For example, we consider a CFDC run from the FIN 02 campaign where Snomax® aerosols were generated by atomization of suspensions and introduced to the AIDA chamber at concentrations of ~2000 cm^{-3}. The CFDC-CASPOL was operated at -15 $^{\circ}C$ ± 1.5 $^{\circ}C$, and scanned from low to high SS_w. A time series of the normalized size distribution is shown in Figure 4a. Figures 4b and c show the mean depolarization ratio of particles larger than 2 μm and CFDC supersaturation (with respect to water and with respect to ice), respectively. Under normal operating conditions, such as those occurring during 10:45 to 11:55 CET (Central European Time Zone), the size distribution is clearly a bimodal distribution with an aerosol population at diameters of ~ 0.5 to 1.5 μm and the ice crystal population at diameters of ~3 to 25 μm. In the figure, water droplet breakthrough is observed between 11:55 to 12:15 CET as the upper limit of the size mode increases from 1.5 to ~10 μm.

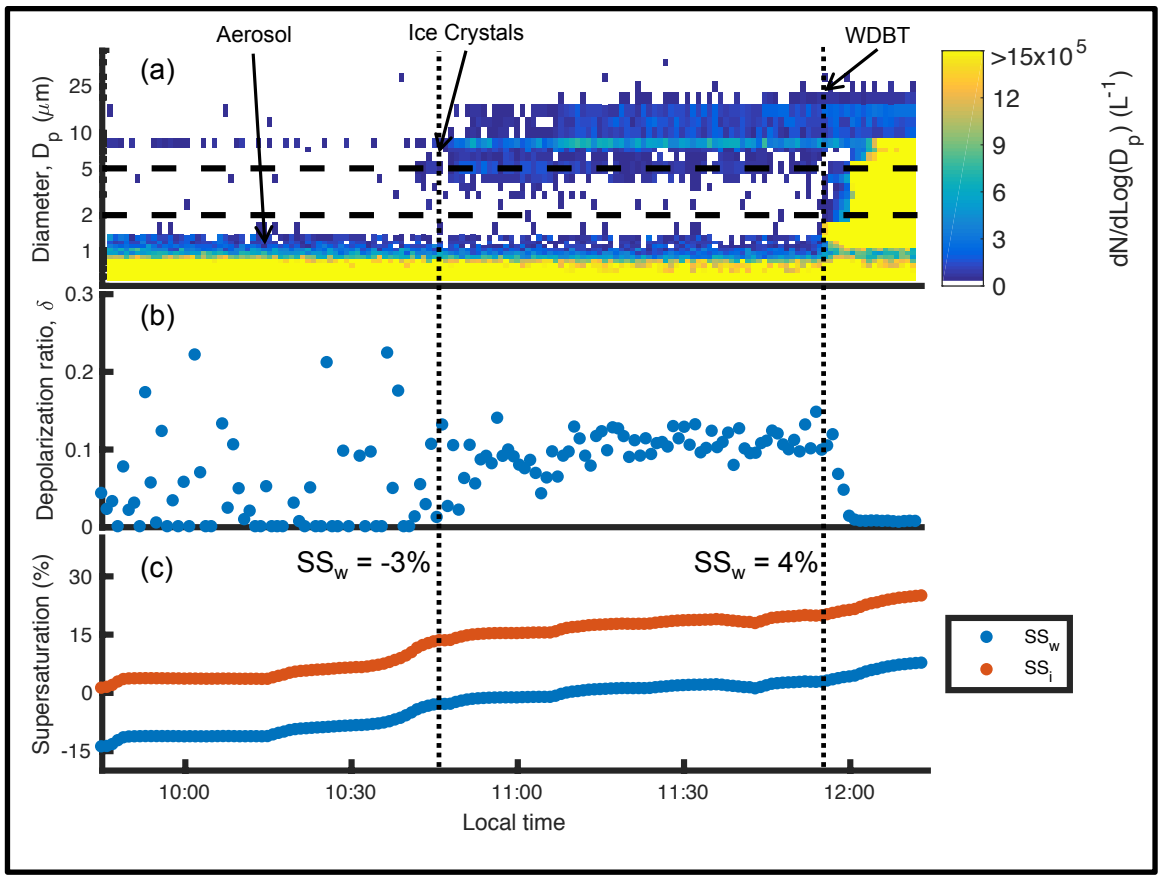

Figure 4. (a) The normalized size distribution, (b) mean depolarization ratio of particles in CFDC with $D_p > 2$ µm, and (c) supersaturation conditions with respect to ice (SS_i) and water (SS_w) for a Snomax scan on March 27 at -15 °C ± 1.5 °C.

In Figure 4b, as ice crystals being to grow in the chamber at higher SS_w, the mean depolarization ratio becomes more uniform, with a range of ~ 0 to 0.22 before 10:45 to a range of ~ 0.09 to 0.12 after 10:45. Then at 11:55 CET (at 4 % SS_w) water droplet breakthrough initiates and the mean depolarization ratio decreases to about zero, consistent with the theoretical depolarization ratio of water droplets. These results show that the mean depolarization ratio of particles larger than 2 µm has a strong dependence

on whether or not WDBT is occurring in the CFDC. This makes the mean depolarization ratio a useful tool that can be used to confirm the onset of water droplet breakthrough.

3.5 Optical properties of particles present in the CFDC

In this section, the depolarization ratio distributions of particles that are present in the CFDC are investigated. In order to do this, it is necessary to interpret the type of particles detected by the CASPOL. First, all data from the FIN 02 campaign was classified as WDBT conditions or normal operating conditions. Then particle diameters are used to determining the particle type. Aerosol particles during the FIN 02 campaign were generally < 2 μm in size. Since water droplets can pollute this population during WDBT conditions, aerosols are interpreted as only those particles that are < 2 μm in diameter during normal operating conditions. Ice crystals are interpreted as particles ≥ 2 μm in diameter during normal operating conditions. A third population is defined as "WDBT particles" and consists of particles ≥ 2 μm in diameter during WDBT conditions. This population typically consists of mostly water droplets, but can also include ice crystals. These three populations are referred to as "CFDC populations" in this manuscript.

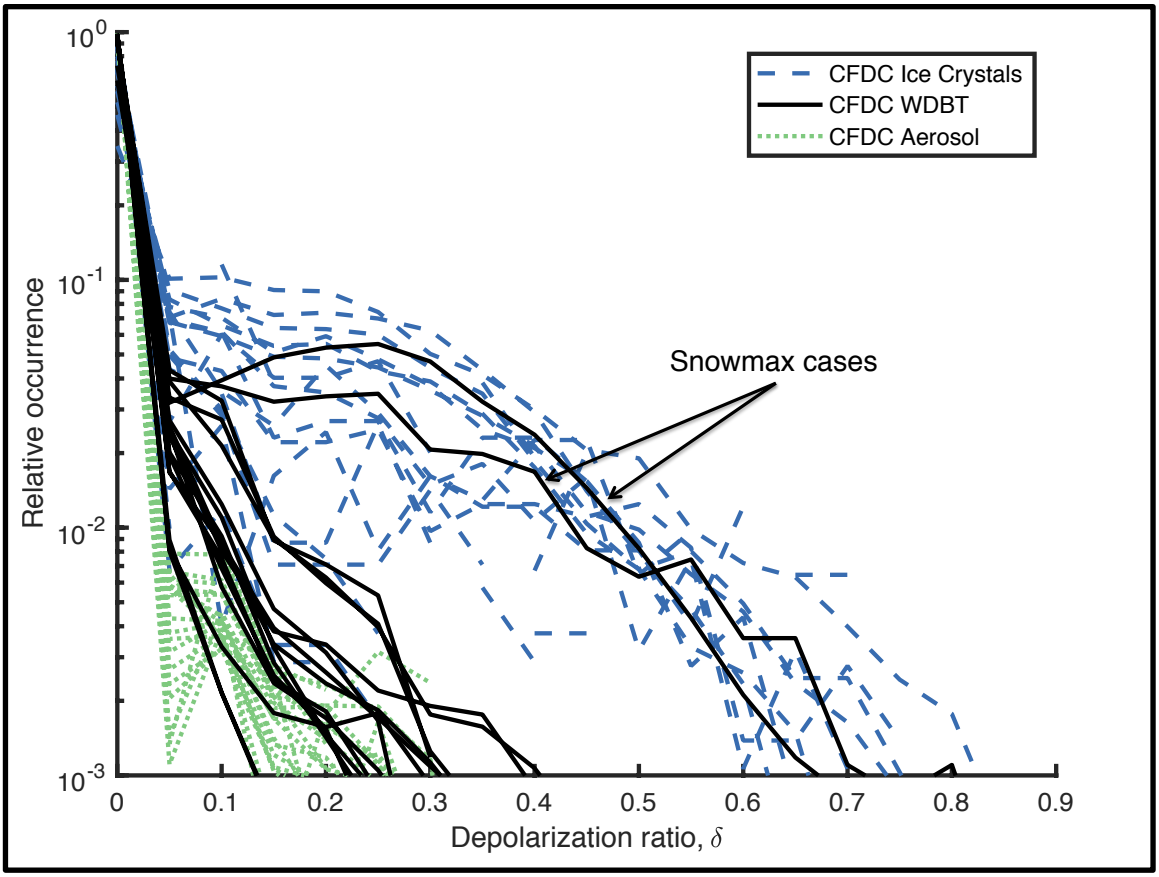

Figure 5. Normalized depolarization ratio distributions for CFDC populations: ice crystal periods (19 periods classified), WDBT periods (17 periods classified), and aerosol periods (19 periods classified).

Figure 5 shows the depolarization ratio distributions of the interpreted CFDC populations for ice crystals, water droplets, and aerosols. For the analysis completed to produce Figure 5, 19 normal operating condition periods and 17 WDBT periods with variable time lengths were classified. Ice crystals achieve higher depolarization ratios than water droplets and aerosol. 13.2 % of ice crystals in the CFDC achieve a depolarization ratio > 0.3, compared to 1.5 % percent of water droplets and 0.3 % of aerosols. These values are very similar to the percentages of training data particles that

achieve a depolarization ratio > 0.3. Ice crystals achieve high depolarization ratios (> 0.3) more than 10 times more frequently than aerosol or water droplets. One interesting feature in the CFDC observations are the two Snomax® (cases 13 and 14 in table 1 at -33 °C and -21 °C respectively) cases in Figure 5. More particles with high depolarization ratios were observed than the other 15 WDBT cases. In Snomax® cases, the distribution of depolarization ratios is similar to that of CFDC ice crystals in non-WDBT periods. Since Snomax® bacteria are a particularly active INP it is not surprising that ice crystals dominate the population of particles in the CFDC even during WDBT (Wex et al., 2015).

3.6 Comparing CASPOL observations to model calculations

In this section, modeled and observed particles discussed in the preceding results section are compared. Figure 6 shows modeled and observed depolarization ratios of particles as a function of diameter. The modeled results (green) are shown with the same shape conventions as Figure 2. Observed results include training (blue shapes) and CFDC (red shapes) ice crystals (pentagrams), aerosols (squares), and droplets/WDBT particles (circles). Observed values are accompanied by error bars representing the standard deviation of depolarization ratios of particles at the respective diameters plotted. The CFDC populations presented here include particles sampled from all FIN 02 experiments. The same conventions are used here to process these particles: CFDC ice crystals are those large than 2 um sample under normal operating conditions, CFDC

aerosols are those smaller than 2 um sampled under normal operating conditions, and CFDC WDBT particles are those larger than 2 um sample under WDBT conditions.

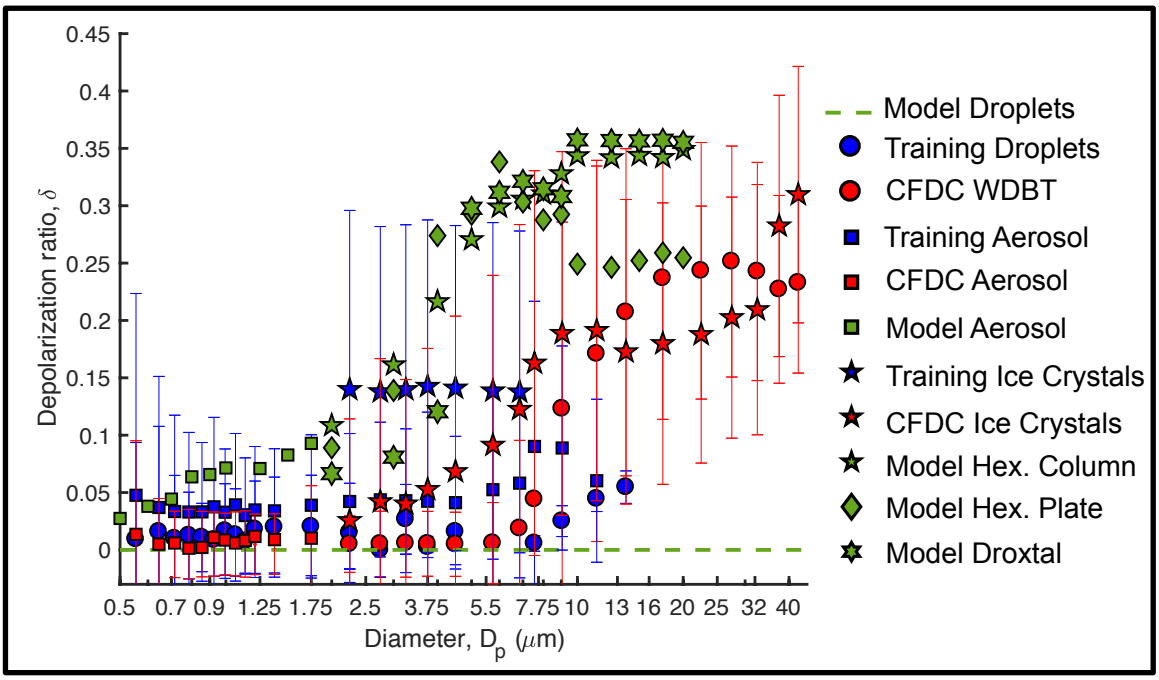

Figure 6. Mean depolarization ratios vs. particle diameter for modeled and observed particles. Observed error bars provide a standard deviation on the depolarization ratios of particles at each reported size. No error bars are reported for model calculations. Model calculations, training populations, and CFDC populations are green, blue, and red respectively. WDBT/droplets are shown as circles, aerosols as squares, and ice crystals as pentagrams, hexagrams, or diamonds.

In Figure 6, both the model calculations and the observed results indicate that ice crystals have higher depolarization ratios than water droplets and aerosols on average at diameters above 5 μm. However, error bars show that the standard deviations of depolarization ratios at these sizes are very large and that the mean depolarization ratios of the observed particles displayed are not statistically significant from each other. This

represents a major challenge in designing a new analysis method that uses depolarization ratio to quantify INP.

In section 3.5, the complex WDBT population was discussed. WDBT particles consist of both water droplets and ice crystals. Diffusional growth theory dictates that ice crystals will grow to larger sizes in the CFDC than water droplets (Pruppacher and Klett, 2012). Figure 6 shows an increase in the depolarization ratio from ~ 0 to 0.25 in the CFDC WDBT region starting at ~6 μm. At diameters > 10 μm the mean depolarization ratio of WDBT particles is greater than or equal to the depolarization of CFDC ice crystals and training dataset ice crystals suggesting that these large particles are mostly or all ice crystals. It's further inferred that particles in the 6 to 10 μm range are a mixture of water droplets and ice crystals.

There are significant differences between modeled particles and their observed counterparts. Observations show water droplets apparently depolarizing light, but the observed mean depolarization ratio of water droplets is almost zero ($\delta \leq 0.05$). Another significant difference is that for both ice crystals and aerosols, the mean observed depolarization ratios are approximately 30% lower than the modeled depolarization ratio. One possible reason for the discrepancies between the model and observations is that the CASPOL depolarization detector underestimates the depolarization of particles due to the weak depolarization of particles and relatively high detection limit of the CASPOL polarization detector. Another possibility is that the idealized model particles do not accurately depict the shape, composition, or other microphysical properties of the observed particles. Smith et al. (2016) found that after an ice crystal has nucleated, the

geometry of the ice crystal can be modified leading to drastic differences in the observed depolarization ratio. To investigate this, Smith et al operated the Manchester Ice Cloud Chamber at different temperatures and supersaturations to produce an assortment of ice crystal morphologies including solid and hollow columns, plates, sectored plates and dendrites. Smith et al. also compared observed and modeled depolarization ratio results and found that on average the difference between modeled and observed depolarization ratios was ~120%. It is also important to note that the range of depolarization ratios for the observed ice crystals spans the entire domain of depolarization ratio (0 to 1) suggesting a wide range of geometries and orientations of ice crystals are sampled with the CASPOL. It's important to note that the CFDC results reported in Figure 6 include data from all of the runs sampled during FIN 02. The data set of the campaign represents ice nucleation events over a broad range of temperature (-15 °C to -35 °C) and supersaturation (0 % to 40 % SS_i) conditions. Thus, many different habits of ice crystals likely formed in the CFDC, in part, contributing to the wide range of depolarization ratios reported in figure 6. Nicolet et al. (2007) reporting modeling results of single-particles that confirm that a wide range of depolarization ratios can be detected for a single shape depending on the orientation. Non-preferential orientation of particles in the CFDC is likely the primary reason for the wide range of depolarization ratios detected. Supplementary Figures S1 – S3 provide box plots that show depolarization ratio distributions vs. particle diameter for the observed particles and provide more detail about the large range of observed depolarization ratios of particles that were sampled by the CFDC-CASPOL.

The observations are qualitatively consistent with the model in that ice crystals depolarize more light than water droplets and aerosols. However, the discrepancies between the observed and modeled mean depolarization ratios and the wide distributions of observed depolarization ratios dictate that we cannot rely on a mean modeled depolarization ratio to identify and quantify ice crystals in the CFDC. Rather than designing a theoretical model based on model calculations, we move forward by designing an empirical model based on the CASPOL observed signals.

3.7 Designing an empirical model to quantify INP with depolarization ratio

The results in Sections 3.2 and 3.3 show that counting ice crystals in the CFDC using depolarization ratio can be challenging since only ~13.5 % of ice crystals achieve a depolarization ratio that is greater than 0.3 (Figures 3 and 5). This 0.3 depolarization ratio threshold is a favorable criterion for ice crystals because < 1% water droplets and aerosols achieve this depolarization ratio. However, during water droplet breakthrough conditions, the water droplet concentration may be 10^3 times greater than the ice crystal concentration in the CFDC effectively reducing the signal to noise ratio ~1:1 or worse. To combat these challenges, we use a linear regression fit derived from a simulated dataset designed with the training data populations described in Sections 2.7 and 3.1. Other work has used a linear regression fit in a similar way to measure $PM_{2.5}$ with a ceilometer backscatter signal (Li et al., 2016).

To design the linear regression model, we create a simulated dataset from the training data populations. This simulated dataset has several segments with variable but

known quantities of ice crystals, water droplets, and aerosols. Second, using the simulated dataset, we optimize the choice of depolarization ratio threshold to maximize retention of ice crystals and removal of water droplet and aerosols. Previous observations reported in this manuscript suggest that 0.3 is an appropriate threshold to quantify ice crystals in the CFDC. Using statistical criteria, we evaluate how well this threshold performs in comparison to other thresholds over a large range of droplet and aerosol concentrations. Finally, we determine a linear regression fit that relates the number of nominally depolarizing particles to the known number of ice crystals in a population determined by the number of ice crystals added from the ice crystal training dataset.

Each simulated dataset is created with 120 segments, with numbers of ice crystals in each segment ranging from 0 to 350. 50 simulated datasets are generated with these identical ice crystal segments, but with incrementally increased droplet and aerosol concentrations. The ratio of water droplets and aerosols is held constant across the 120 segments in a simulated dataset. The quantity of aerosols in each simulated dataset is dictated by the multiplication factor M, where the water droplet concentration = $100M$ and the aerosol concentration = $300M$. The multiplication factor, M, increases by 1 for each iteration of the simulated dataset, ranging from 1 to 50, resulting in ranges of numbers of water droplets and aerosols of 100 to 5,000 and 300 to 15,000 respectively. The droplet, aerosol, and ice crystal training datasets are randomized in time before the particles are selected from each population to form the simulated dataset. After these 50 simulated datasets are generated, the number of particles greater than or equal to a

selected depolarization ratio threshold (ranging from 0 to 0.75 in increments of 0.05) and that are larger than 2 μm is determined for each of the 120 segments in the simulated dataset. A linear fit is determined for the relationship between the known ice crystal concentration and the number of particles detected greater than or equal to the depolarization ratio threshold for only the simulated datasets generated where $M = 1$. The linear regression fit determined is then applied to all of the simulated datasets over the entire range of M. Only one fit is determined for each threshold because we cannot feasibly design a model that adapts to water droplet and aerosol concentration in the CFDC. An R^2 value is determined to assess the fitness of the linear regression over all of the simulated datasets.

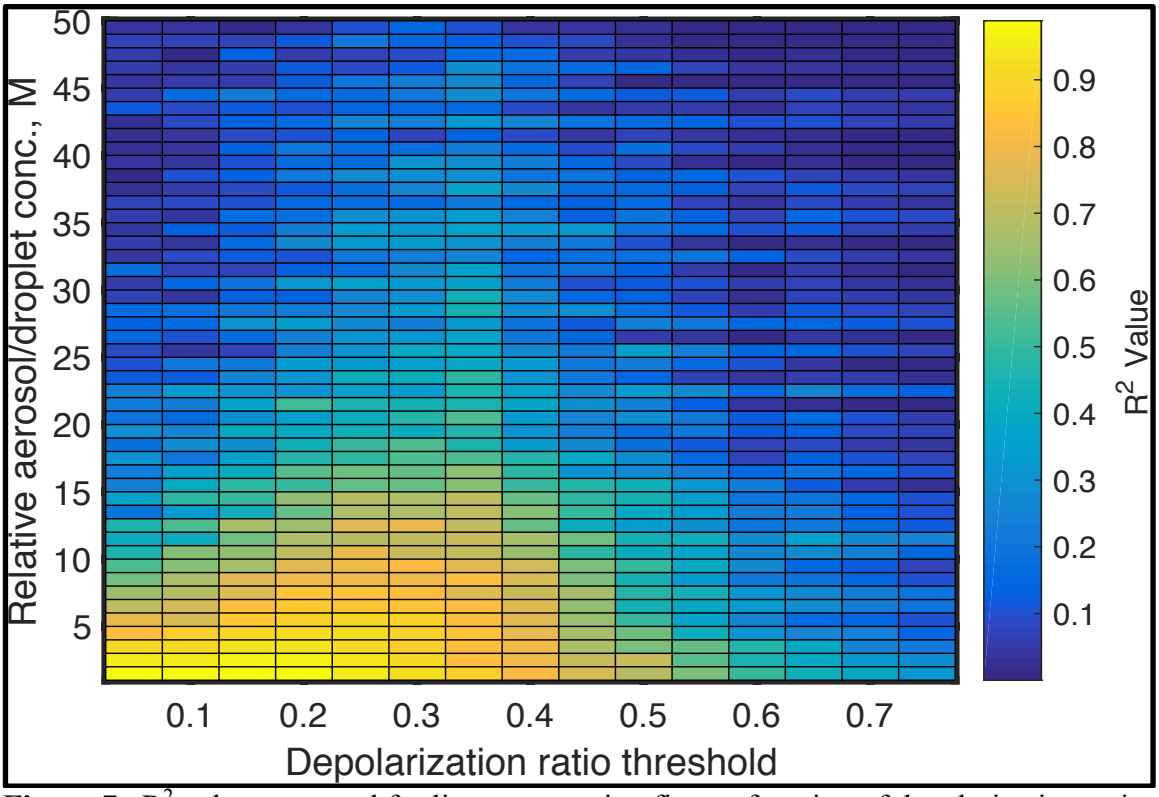

Figure 7. R^2 values reported for linear regression fit as a function of depolarization ratio threshold and water droplet/aerosol concentration multiplication factor, M.

Figure 7 shows the R^2 values as a function of *M* and depolarization ratio threshold for each for each of the simulated datasets. The figure shows that R^2 values are very accurate for cases where aerosol and droplet concentrations are low and when the depolarization ratio threshold is low. However, as the concentration of droplets and aerosol increase, the R^2 value decreases. This is especially true for lower depolarization ratio thresholds that are more sensitive to increases in droplet and aerosols. An optimal choice for depolarization ratio threshold is defined as a threshold that retains relatively high R^2 values across the entire range of *M*. Figure 7 shows that the 0.3 and 0.35 thresholds are both optimal choices. However, aerosol and water droplet concentrations

in CFDC experiments are typically in in the range $1< M< 20$. The mean R^2 value in this range of M for the 0.3 and 0.35 thresholds 0.71 and 0.7 respectively. Thus we confirm that the 0.3 depolarization ratio threshold is the most appropriate threshold. The linear regression for the 0.3 threshold is provided in Eq. (9),

$$N_{INP} = 6.11\, N_{\delta} + 22.20 \quad (9)$$

where N_{δ} is the number of particles that have a depolarization ratio greater than 0.3 and N_{INP} is the derived INP number. Eq. (9) will be applied to all CFDC-CASPOL data collected during the FIN 02 campaign and the accuracy of this model will be determined.

3.8 Application of the new analysis method to CFDC data collected during FIN 02

INP concentrations were obtained using both the depolarization ratio method (Eq. (9)) and the traditional method on CFDC data collected during the FIN 02 campaign. Three representative CFDC runs of Snomax® (a & b) and Arizona test dust (c) are shown in Figure 8. Each scan starts in subsaturated conditions with respect to water. Supersaturation is gradually increased until ice nucleation initiates and then further increased until WDBT occurs (represented by the red points in (b)). The reported concentrations reveal that the traditional and depolarization ratio methods generally agree during "ice only" periods (blue symbols in (b)). In most cases there is disagreement between concentrations in WDBT periods. This is expected since the traditional concentration is sensitive to an increase in water droplets that grow larger than the size cut applied in WDBT conditions, where INP concentrations are usually not reported. An exception to this can be seen in Figure 8b, the Snomax® case discussed

above. The concentrations from both methods seem to agree in this WDBT period. This is because in this case, the ice crystal concentration is dominating the population in WDBT and the SS_w is not highly elevated. The evidence for this is the high concentration of ice crystals that form the period that starts around 13:15 CET as observed in the size distribution time series in bottom panel of Figure 8b.

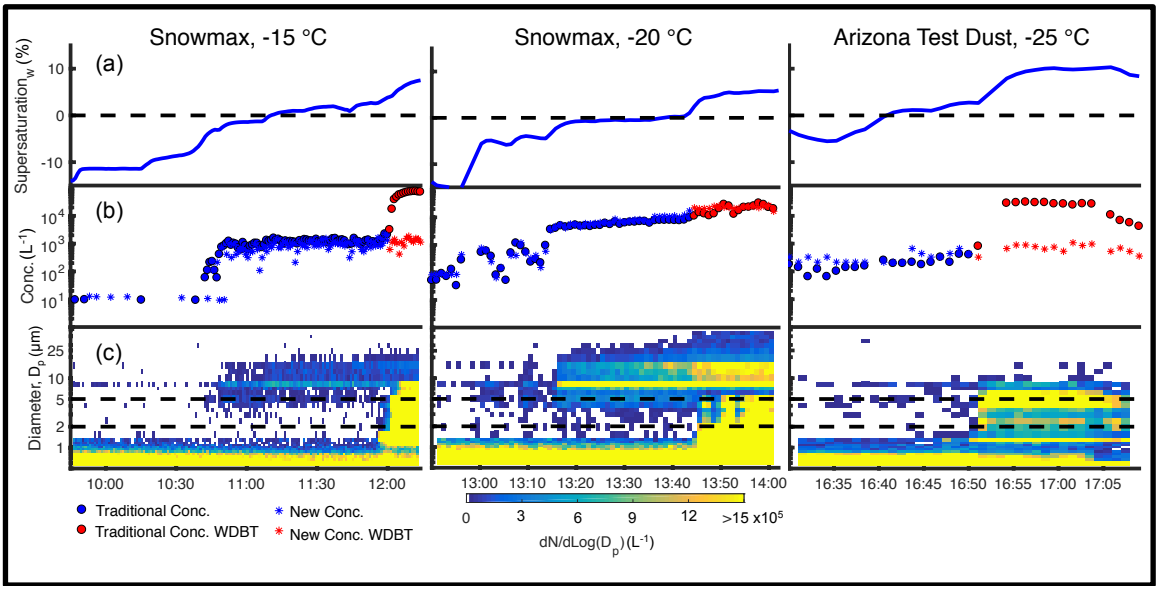

Figure 8. Application of depolarization ratio method on three CFDC runs. Aerosol composition and temperature are labelled in the title. Time series are shown for (a) supersaturation with respect to water, (b) traditional and new INP concentrations under normal operating conditions and WDBT conditions (see legend), and (c) the log-normal size distribution. Time is reported in local time (CET).

Figure 9 summarizes the mean concentrations obtained through the traditional and new method for all periods when the CFDC was operational during FIN 02. In total, 27 "ice only" periods and WDBT cases are included. A description of the date and time,

aerosol composition, and temperature of each case is detailed in Table 1. The error bars report the CASPOL uncertainty, which is 39%. Figure 9 shows that in all but 4 cases out of 27 (cases 2, 7, 9, and 23), the mean concentration of the new analysis method lies is in agreement with traditional analysis method for the "ice only" periods. Figure 9 also shows that only 9 out of 24 WDBT cases have statistical agreement between the new and traditional analysis method. It should be noted that in most of the WDBT cases that have agreement, this is due to the large variation of the traditional concentration during that time period. At the onset of WDBT, the impact of water droplets on the 2 μm cut concentration may not be very large and the concentration may closely resemble the true INP concentration, but as the SS_w is increased more water droplets will be incorrectly counted towards the traditional INP concentration. This phenomenon gives rise to the large error bars reported in some of the WDBT cases. The only WDBT cases that have reasonably similar concentrations from both new and traditional methods are cases 13, 14, and 19.These specific cases are those where there are high concentrations of ice crystals and relatively low concentrations of large water droplets. In general, the observations reported in Figure 9 are consistent with the assertion that the traditional method and new method are in agreement during the "ice only" periods and that during WDBT the traditional method is elevated in response to large water droplets polluting the INP concentration while the depolarization ratio method remains at a reasonable concentration for INP that we speculate is accurate.

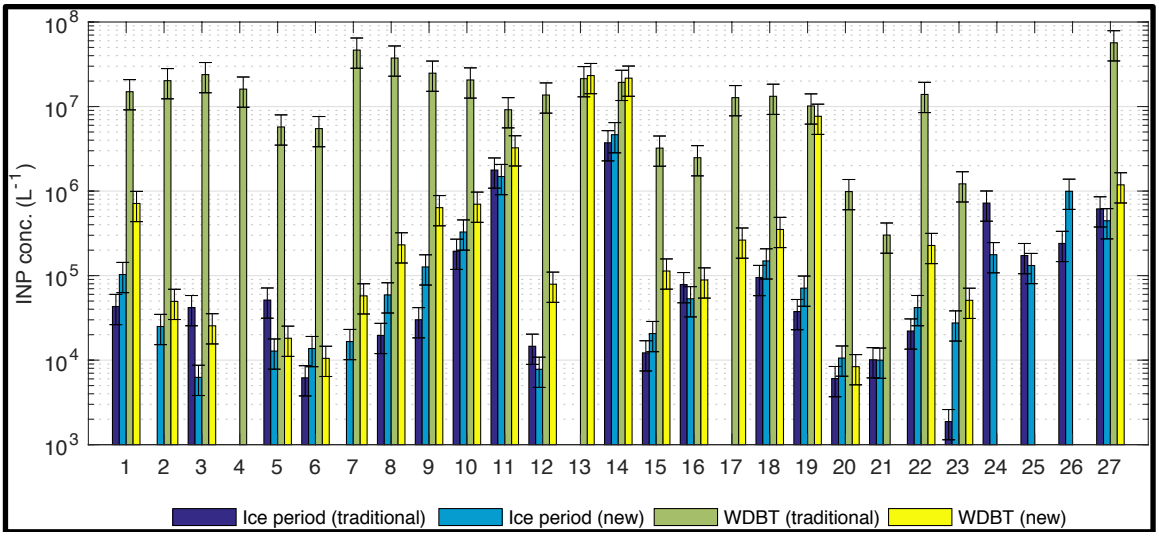

Figure 9. Individual cases of "Ice Only" and "WDBT" concentration comparisons with the traditional size-cut and depolarization ratio methods. Error bars report the CFDC-CASPOL counting error of 39%.

To summarize the comparison between our new method and the traditional method during the "ice only" periods, the INP concentrations determined using the traditional method vs. new method is plotted in Figure 10a. Each point on the plot represents data for a 1-minute segment. The black line in Figure 10 is a 1:1 line. Since the analysis used to generate Figure 10 only uses data collected under normal operating conditions (not WDBT), the traditional concentration can be considered ground truth. The data closely follows the 1:1 line, confirming that the depolarization ratio can be used to reliably retrieve an INP concentration when no or few water droplets/aerosols are larger than 2 μm. The mean percent error of the method is dependent on the INP concentration. Due to the high detection limit of concentration for the CASPOL, the mean percent error of the new method is ±500% when the traditional concentration is between 0 and 50,000 L^{-1}. However, at higher concentrations the MPE is typically ± 50

% or less. Additionally, figure 10b shows that at lower concentrations (0 to 3 × 10^6 L^{-1}) the new method typically undercounts INP, but over counts INP at higher concentrations (> 3 × 10^6 L^{-1}). The mean percent error for the new method for all concentrations is ± 32.1 %.

Based on Figure 10, the new analysis method only provides a reasonable result when INP concentrations are relatively high, which is only achievable in laboratory settings. For this reason, the method is not suitable to be used in a field setting where concentrations typically range from 0.1 to 100 L^{-1} (e.g. Mason et al., 2016; Jiang et al., 2015; DeMott et al., 2003). Therefore, the new method will not be adopted as standard procedure. Nonetheless, the new method will be considered an improvement if it can be used during water droplet breakthrough, when the traditional method cannot be used.

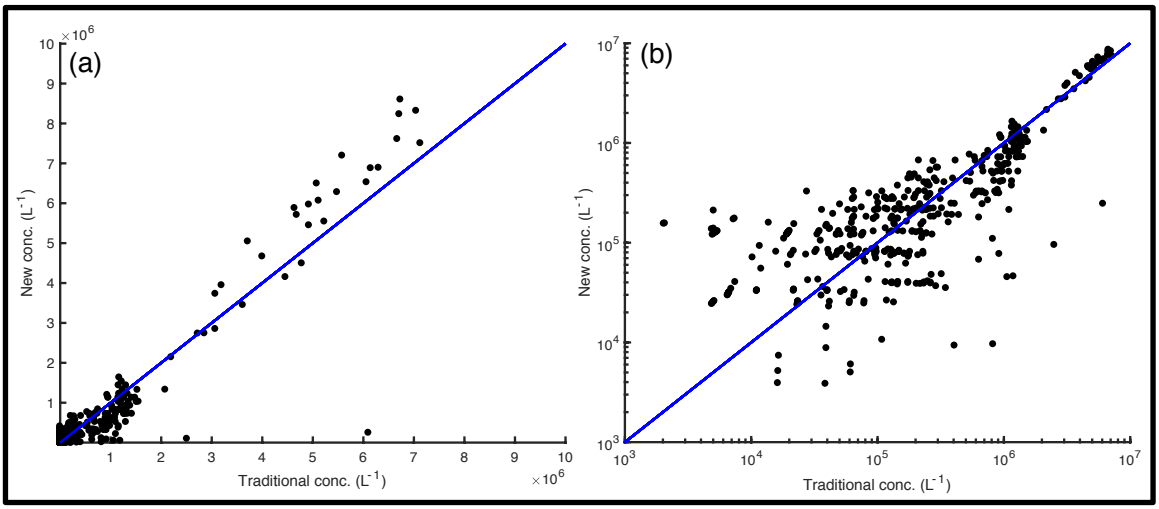

Figure 10. Traditional concentration vs. new concentration with 1:1 line for "ice only" periods. (a) Linear scale and (b) log-log scale are reported.

In order to determine if the method is successful during water droplet breakthrough periods, we need a reliable measure of INP to compare to at higher supersaturation conditions (when the TAMU CFDC is experiencing WDBT). Due to design and flow rate differences, the Colorado State University (CSU) CFDC does not experience the onset of WDBT until higher supersaturations compared to the TAMU CFDC, up to 108% or higher depending on temperature (DeMott et al., 2015). Figure 11 shows the comparison of the TAMU CFDC's traditional and new INP concentrations and the CSU CFDC INP concentration. Concentrations reported are average concentrations of samples in a 1% range of SS_w conditions in the CFDC. Because the CSU CFDC has a different detector than the TAMU CFDC, CSU reports an INP concentration using a nominal size cut of 3 μm. Though not previously discussed in the manuscript, a 5 μm has also been used to report an INP concentration for the TAMU CFDC and is used here to provide upper and lower estimates for the INP concentration. Results of INP fraction activated from three CFDC runs are reported for Snowmax at -15 $^{\circ}$C and -20 $^{\circ}$C and Arizona test dust at -25 $^{\circ}$C. Large symbols show data collected under normal operating conditions. The CFDC runs reported in Figures 11 a, b, and c correspond to the cases reported in Figures 8 a, b, and c respectively. Small symbols show data collected during WDBT conditions in the TAMU CFDC. The CSU CFDC did not experience WDBT in the data reported in Figure 11. The traditional concentration from TAMU and CSU and the new method concentration all are in reasonable agreement during "ice only" conditions. When WDBT occurs, the TAMU traditional concentrations increase in response to the water droplets that grow larger than the size

criteria (2 µm or 5 µm), however, the new method remains in agreement with the CSU concentration, which is not experiencing WDBT. In conclusion, the new method can accurately determine the INP concentration in the presence of water droplets and can thus extend the range of operating conditions of the TAMU CFDC.

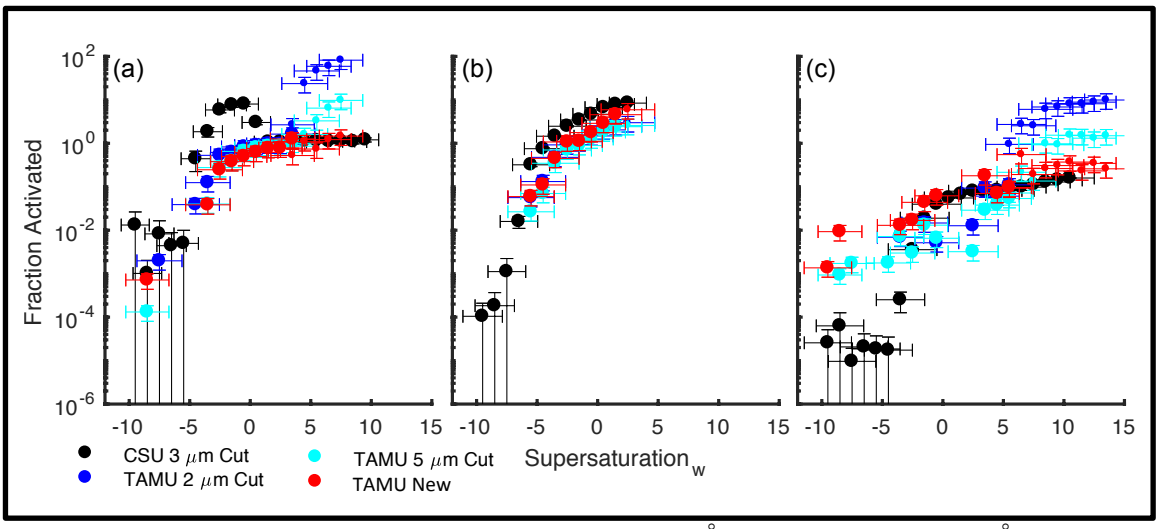

Figure 11. CSU TAMU comparison: Snomax at -15 °C (a), Snomax at -20 °C (b), and Arizona Test Dust at -25 °C (c). Small symbols indicate that those points were sampled in WDBT. TAMU 2 µm cut and 5 µm cut traditional INP fraction activated are shown in blue and cyan respectively. The TAMU new analysis method INP fraction activated is shown in red. The CSU 3 µm INP fraction activated is shown in black.

4. CONCLUSIONS

This manuscript presents a new analysis method that uses depolarization ratio to quantify INP concentrations in a CFDC using single-particle depolarization. Ice crystal, droplet and aerosol training populations were used to build simulated datasets with known concentrations of aerosols, droplets, and ice crystals. The simulated datasets were evaluated to determine the optimal depolarization ratio threshold used to determine INP concentrations in the TAMU CFDC, as 0.3. Next, an empirical model was designed using a linear regression fit that was trained on simulated CFDC dataset using the 0.3 threshold. This model was applied to the CFDC data collected during the FIN 02 campaign. Concentrations of INP determined by the new analysis method agree reasonably well with the traditional method under normal operating conditions with a mean percent error of ±32.1 %. However at INP concentrations <50,000 L^{-1}, the mean percent error of the new method is > 500 % due to a high concentration detection limit of the CASPOL during CFDC operation (~5,000 L^{-1}). While high INP concentrations of 10^4 to 10^6 L^{-1} can be generated in laboratory settings, typical ambient INP concentrations range from 0 to 100 L^{-1}. For this reason, the current configuration of the CASPOL instrument is not suitable for field measurements. A comparison between the CSU CFDC INP concentration and TAMU CFDC INP concentration derived from the new analysis method show agreement even under conditions in which the TAMU CFDC is experiencing WDBT and CSU is not experiencing WDBT. We conclude that the new

method can be used to extend the range of operating conditions in the CFDC. However, under normal operating conditions, the traditional method is still the most appropriate analysis method to employ.

REFERENCES

Amato, P., Joly, M., Schaupp, C., Attard, E., Möhler, O., Morris, C., Brunet, Y. & Delort, A.-M. 2015. Survival and Ice Nucleation Activity of Bacteria as Aerosols in a Cloud Simulation Chamber. *Atmospheric Chemistry and Physics,* 15**,** 6455-6465.

Atkinson, J. D., Murray, B. J., Woodhouse, M. T., Whale, T. F., Baustian, K. J., Carslaw, K. S., Dobbie, S., O'sullivan, D. & Malkin, T. L. 2013. The Importance of Feldspar for Ice Nucleation by Mineral Dust in Mixed-Phase Clouds. *Nature,* 498**,** 355-358.

Bailey, M. P. & Hallett, J. 2009. A Comprehensive Habit Diagram for Atmospheric Ice Crystals: Confirmation from the Laboratory, Airs Ii, and other Field Studies. *Journal of the Atmospheric Sciences,* 66**,** 2888-2899.

Bi, L., Yang, P., Kattawar, G. W. & Mishchenko, M. I. 2013. Efficient Implementation of the Invariant Imbedding T-Matrix Method and the Separation of Variables Method Applied to Large Nonspherical Inhomogeneous Particles. *Journal of Quantitative Spectroscopy and Radiative Transfer,* 116**,** 169-183.

Boucher, O., Randall, D., Artaxo, P., Bretherton, C., Feingold, G., Forster, P., Kerminen, V.-M., Kondo, Y., Liao, H., Lohmann, U., Rasch, P., Satheesh, S. K., Sherwood, S., Stevens, B. & Zhang, X. Y. 2013. Clouds and Aerosols. *in:* Stocker, T. F., Qin, D., Plattner, G.-K., Tignor, M., Allen, S. K., Boschung, J., Nauels, A., Xia, Y., Bex, V. & Midgley, P. M. (Eds.) *Climate Change 2013: The Physical Science Basis. Contribution of Working Group I to the Fifth Assessment Report of the Intergovernmental Panel on Climate Change.* Cambridge, United Kingdom and New York, NY, USA: Cambridge University Press.

Clauss, T., Kiselev, A., Hartmann, S., Augustin, S., Pfeifer, S., Niedermeier, D., Wex, H. & Stratmann, F. 2013. Application of Linear Polarized Light for the Discrimination of Frozen and Liquid Droplets in Ice Nucleation Experiments. *Atmospheric Measurement Techniques,* 6**,** 1041-1052.

Collier, K. N. & Brooks, S. D. 2016. Role of Organic Hydrocarbons in Atmospheric Ice Formation via Contact Freezing. *The Journal of Physical Chemistry A*. *120* (51), 10169-10180

Creamean, J. M., Suski, K. J., Rosenfeld, D., Cazorla, A., Demott, P. J., Sullivan, R. C., White, A. B., Ralph, F. M., Minnis, P. & Comstock, J. M. 2013. Dust and Biological Aerosols from the Sahara and Asia Influence Precipitation in the Western US. *Science,* 339**,** 1572-1578.

De Boer, G., Morrison, H., Shupe, M. & Hildner, R. 2011. Evidence of Liquid Dependent Ice Nucleation in High-Latitude Stratiform Clouds from Surface Remote Sensors. *Geophysical Research Letters,* 38.

Demott, P. J., Hill, T. C., Mccluskey, C. S., Prather, K. A., Collins, D. B., Sullivan, R. C., Ruppel, M. J., Mason, R. H., Irish, V. E. & Lee, T. 2016. Sea Spray Aerosol as a Unique Source of Ice Nucleating Particles. *Proceedings of the National Academy of Sciences,* 113**,** 5797-5803.

Demott, P. J., Möhler, O., Stetzer, O., Vali, G., Levin, Z., Petters, M. D., Murakami, M., Leisner, T., Bundke, U. & Klein, H. 2011. Resurgence in Ice Nuclei Measurement Research. *Bulletin of the American Meteorological Society,* 92**,** 1623-1635.

Demott, P. J., Prenni, A. J., Mcmeeking, G. R., Sullivan, R. C., Petters, M. D., Tobo, Y., Niemand, M., Möhler, O., Snider, J. R. & Wang, Z. 2015. Integrating Laboratory and Field Data to Quantify the Immersion Freezing Ice Nucleation Activity of Mineral Dust Particles. *Atmospheric Chemistry and Physics,* 15**,** 393-409.

Demott, P. J., Sassen, K., Poellot, M. R., Baumgardner, D., Rogers, D. C., Brooks, S. D., Prenni, A. J. & Kreidenweis, S. M. 2003. African Dust Aerosols as Atmospheric Ice Nuclei. *Geophysical Research Letters,* 30.

Durant, A. J. & Shaw, R. A. 2005. Evaporation Freezing by Contact Nucleation Inside-Out. *Geophysical Research Letters,* 32.

Fornea, A. P., Brooks, S. D., Dooley, J. B. & Saha, A. 2009. Heterogeneous Freezing of Ice on Atmospheric Aerosols Containing Ash, Soot, and Soil. *Journal of Geophysical Research: Atmospheres,* 114.

Garimella, S., Kristensen, T., Ignatius, K., Welti, A., Voigtländer, J., Kulkarni, G., Sagan, F., Kok, G., Dorsey, J. & Nichman, L. 2016. The Spectrometer for Ice Nuclei (SPIN): An Instrument to Investigate Ice Nucleation, Atmos. *Meas. Tech. Discuss., Do I,* 10.

Glen, A. & Brooks, S. 2013. A New Method For Measuring Optical Scattering Properties of Atmospherically Relevant Dusts Using the Cloud and Aerosol Spectrometer with Polarization (CASPOL). *Atmospheric Chemistry and Physics,* 13**,** 1345-1356.

Glen, A. & Brooks, S. D. 2014. Single Particle Measurements of the Optical Properties of Small Ice Crystals and Heterogeneous Ice Nuclei. *Aerosol Science and Technology,* 48**,** 1123-1132.

Glen, A. 2014. *The Development of Measurement Techniques to Identify and Characterize Dusts and Ice Nuclei in the Atmosphere.* Texas A&M University.

Hoose, C. & Möhler, O. 2012. Heterogeneous Ice Nucleation on Atmospheric Aerosols: A Review of Results from Laboratory Experiments. *Atmos. Chem. Phys,* 12**,** 9817-9854.

Hu, Y., Winker, D., Vaughan, M., Lin, B., Omar, A., Trepte, C., Flittner, D., Yang, P., Nasiri, S. L. & Baum, B. 2009. CALIPSO/CALIOP Cloud Phase Discrimination Algorithm. *Journal of Atmospheric and Oceanic Technology,* 26**,** 2293-2309.

Jiang, H., Yin, Y., Yang, L., Yang, S., Su, H. & Chen, K. 2014. The Characteristics of Atmospheric Ice Nuclei Measured at Different Altitudes in the Huangshan Mountains in Southeast China. *Advances in Atmospheric Sciences,* 31**,** 396 0256-1530.

Levin, E., Mcmeeking, G., Demott, P., Mccluskey, C., Carrico, C., Nakao, S., Jayarathne, T., Stone, E., Stockwell, C. & Yokelson, R. 2016. Ice-Nucleating Particle Emissions from Biomass Combustion and the Potential Importance of Soot Aerosol. *Journal of Geophysical Research: Atmospheres*.

Li, S., Joseph, E. & Min, Q. 2016. Remote Sensing of Ground-Level PM2. 5 Combining AOD and Backscattering Profile. *Remote Sensing of Environment,* 183**,** 120-128.

Linke, C., Möhler, O., Veres, A., Mohacsi, A., Bozóki, Z., Szabó, G. & Schnaiter, M. 2006. Optical Properties and Mineralogical Composition of Different Saharan Mineral Dust Samples: A Laboratory Study. *Atmospheric Chemistry and Physics,* 6**,** 3315-3323.

Liu, C., Panetta, R. L., Yang, P., Macke, A. & Baran, A. J. 2013. Modeling the Scattering Properties of Mineral Aerosols Using Concave Fractal Polyhedra. *Applied Optics,* 52**,** 640-652.

Marcolli, C. 2014. Deposition Nucleation Viewed As Homogeneous Or Immersion Freezing in Pores and Cavities. *Atmospheric Chemistry and Physics,* 14**,** 2071-2104.

Mason, R. H., Si, M., Chou, C., Irish, V., Dickie, R., Elizondo, P., Wong, R., Brintnell, M., Elsasser, M. & Lassar, W. 2016. Size-Resolved Measurements of Ice-Nucleating Particles at Six Locations in North America and One in Europe. *Atmospheric Chemistry and Physics,* 16**,** 1637-1651.

Mccluskey, C. S., Demott, P. J., Prenni, A. J., Levin, E. J., Mcmeeking, G. R., Sullivan, A. P., Hill, T. C., Nakao, S., Carrico, C. M. & Kreidenweis, S. M. 2014. Characteristics of Atmospheric Ice Nucleating Particles Associated With Biomass Burning in the Us: Prescribed Burns and Wildfires. *Journal of Geophysical Research: Atmospheres,* 119**,** 10458-10470.

Mccluskey, C. S., Hill, T. C., Malfatti, F., Sultana, C. M., Lee, C., Santander, M. V., Beall, C. M., Moore, K. A., Cornwell, G. C. & Collins, D. B. 2016. A Dynamic Link Between Ice Nucleating Particles Released in Nascent Sea Spray Aerosol and Oceanic Biological Activity During Two Mesocosm Experiments. *Journal of the Atmospheric Sciences*.

Mcfarquhar, G. M., Ghan, S., Verlinde, J., Korolev, A., Strapp, J. W., Schmid, B., Tomlinson, J. M., Wolde, M., Brooks, S. D. & Cziczo, D. 2011. Indirect and Semi-Direct Aerosol Campaign: The Impact of Arctic Aerosols on Clouds. *Bulletin of the American Meteorological Society,* 92**,** 183-201.

Mishchenko, M. I. & Sassen, K. 1998. Depolarization of Lidar Returns By Small Ice Crystals: An Application to Contrails. *Geophysical Research Letters,* 25**,** 309-312.

Murray, B., O'sullivan, D., Atkinson, J. & Webb, M. 2012. Ice Nucleation By Particles Immersed in Supercooled Cloud Droplets. *Chemical Society Reviews,* 41**,** 6519-6554.

Nicolet, M., Stetzer, O. & Lohmann, U. 2007. Depolarization Ratios of Single Ice Particles Assuming Finite Circular Cylinders. *Applied Optics,* 46**,** 4465-4476.

Nicolet, M., Stetzer, O., Lüönd, F., Möhler, O. & Lohmann, U. 2010. Single Ice Crystal Measurements During Nucleation Experiments With the Depolarization Detector Iode. *Atmospheric Chemistry and Physics,* 10**,** 313-325.

Niemand, M., Möhler, O., Vogel, B., Vogel, H., Hoose, C., Connolly, P., Klein, H., Bingemer, H., Demott, P. & Skrotzki, J. 2012. A Particle-Surface-Area-Based Parameterization of Immersion Freezing on Desert Dust Particles. *Journal of the Atmospheric Sciences,* 69**,** 3077-3092.

Noel, V. & Sassen, K. 2005. Study of Planar Ice Crystal Orientations in Ice Clouds from Scanning Polarization Lidar Observations. *Journal of Applied Meteorology,* 44**,** 653-664.

Prenni, A., Tobo, Y., Garcia, E., Demott, P., Huffman, J., Mccluskey, C., Kreidenweis, S., Prenni, J., Pöhlker, C. & Pöschl, U. 2013. the Impact of Rain on Ice Nuclei Populations at A Forested Site in Colorado. *Geophysical Research Letters,* 40**,** 227-231.

Rogers, D. C. 1988. Development of A Continuous Flow Thermal Gradient Diffusion Chamber For Ice Nucleation Studies. *Atmospheric Research,* 22**,** 149-181.

Rogers, D. C., Demott, P. J., Kreidenweis, S. M. & Chen, Y. 2001. A Continuous-Flow Diffusion Chamber For Airborne Measurements of Ice Nuclei. *Journal of Atmospheric and Oceanic Technology,* 18**,** 725-741.

Schnaiter, M., Järvinen, E., Vochezer, P., Abdelmonem, A., Wagner, R., Jourdan, O., Mioche, G., Shcherbakov, V. N., Schmitt, C. G. & Tricoli, U. 2016. Cloud Chamber Experiments on the Origin of Ice Crystal Complexity in Cirrus Clouds. *Atmospheric Chemistry and Physics,* 16**,** 5091-5110.

Smith, H. R., Connolly, P. J., Webb, A. R. & Baran, A. J. 2016. Exact and Near Backscattering Measurements of the Linear Depolarisation Ratio of Various Ice Crystal Habits Generated in A Laboratory Cloud Chamber. *Journal of Quantitative Spectroscopy and Radiative Transfer,* 178**,** 361-378.

Vali, G. 1985. Nucleation Terminology. Amer Meteorological Soc 45 Beacon St, Boston, Ma 02108-3693.

Vali, G., Demott, P., Möhler, O. & Whale, T. 2015. Technical Note: A Proposal For Ice Nucleation Terminology. *Atmospheric Chemistry and Physics,* 15**,** 10263-10270.

Wagner, R., Höhler, K., Möhler, O., Saathoff, H. & Schnaiter, M. 2015. Crystallization and Immersion Freezing Ability of Oxalic and Succinic Acid in Multicomponent Aqueous Organic Aerosol Particles. *Geophysical Research Letters,* 42**,** 2464-2472.

Wendisch, M., Pilewskie, P., Pommier, J., Howard, S., Yang, P., Heymsfield, A. J., Schmitt, C. G., Baumgardner, D. & Mayer, B. 2005. Impact of Cirrus Crystal

Shape on Solar Spectral Irradiance: A Case Study For Subtropical Cirrus. *Journal of Geophysical Research: Atmospheres,* 110.

Wylie, D. P. & Menzel, W. P. 1999. Eight Years of High Cloud Statistics Using Hirs. *Journal of Climate,* 12**,** 170-184.

Yakobi-Hancock, J., Ladino, L. & Abbatt, J. 2013. Feldspar Minerals As Efficient Deposition Ice Nuclei. *Atmospheric Chemistry and Physics,* 13**,** 11175-11185.

Yang, P. & Liou, K. 1996. Geometric-Optics–Integral-Equation Method For Light Scattering By Nonspherical Ice Crystals. *Applied Optics,* 35**,** 6568-6584.

Yang, P., Liou, K.-N., Bi, L., Liu, C., Yi, B. & Baum, B. A. 2015. On the Radiative Properties of Ice Clouds: Light Scattering, Remote Sensing, and Radiation Parameterization. *Advances in Atmospheric Sciences,* 32**,** 32-63.

Yoshida, R., Okamoto, H., Hagihara, Y. & Ishimoto, H. 2010. Global Analysis of Cloud Phase and Ice Crystal Orientation from Cloud-Aerosol Lidar and Infrared Pathfinder Satellite Observation (Calipso) Data Using Attenuated Backscattering and Depolarization Ratio. *Journal of Geophysical Research: Atmospheres,* 115.

Zhang, Y., Macke, A. & Albers, F. 1999. Effect of Crystal Size Spectrum and Crystal Shape on Stratiform Cirrus Radiative Forcing. *Atmospheric Research,* 52**,** 59-75.

Zolles, T., Burkart, J., HäUsler, T., Pummer, B., Hitzenberger, R. & Grothe, H. 2015. Identification of Ice Nucleation Active Sites on Feldspar Dust Particles. *The Journal of Physical Chemistry A,* 119**,** 2692-2700.

APPENDIX A

Table A-1 Details of the samples collected during the FIN 02 campaign. This table reports the date and time (CET) that a case was samples, the compositions of aerosol sampled, the chamber that the TAMU CFDC sampled and the temperature (± 1.5 °C) that the CFDC was set to.

Case	Date Time	Composition	Chamb	Temperature
1	3/24/15	Arizona Test Dust	AIDA	-25
2	3/24/15	Arizona Test Dust	AIDA	-20
3	3/24/15	Arizona Test Dust	APC	-19
4	3/24/15	Argentinian Soil	AIDA	-19
5	3/24/15	Argentinian Soil	AIDA	-18
6	3/24/15	Argentinian Soil	AIDA	-24
7	3/25/15	Argentinian Soil	AIDA	-25
8	3/25/15	Argentinian Soil	AIDA	-28
9	3/25/15	Argentinian Soil	APC	-28
10	3/25/15	Arizona Test Dust	AIDA	-25
11	3/25/15	Arizona Test Dust	AIDA	-28
12	3/19/15	Arizona Test Dust	AIDA	-34
13	3/20/15	Snomax	APC	-33
14	3/20/15	Snomax	APC	-21
15	3/21/15	Snomax	AIDA	-16
16	3/21/15	Snomax	AIDA	-19
17	3/21/15	Snomax	AIDA	-20
18	3/21/15	Snomax	APC	-15
19	3/23/15	K-Feldspar	AIDA	-30
20	3/23/15	Blank	AIDA	-25
21	3/23/15	Blank	AIDA	-21
22	3/26/15	Illite NX	AIDA	-25
23	3/26/15	Illite NX	AIDA	-25
24	3/26/15	Illite NX	AIDA	-28
25	3/26/15	Illite NX	AIDA	-30
26	3/26/15	Desert Dust	APC	-29
27	3/27/15	Snomax	APC	-16

APPENDIX B

In Figures 12-14, the red line reports the median, the blue box represents the quartile range, the black dashed whiskers have a length of 1.5 if the inner quartile range, and the red crosses are any points that lie outside of the whiskers.

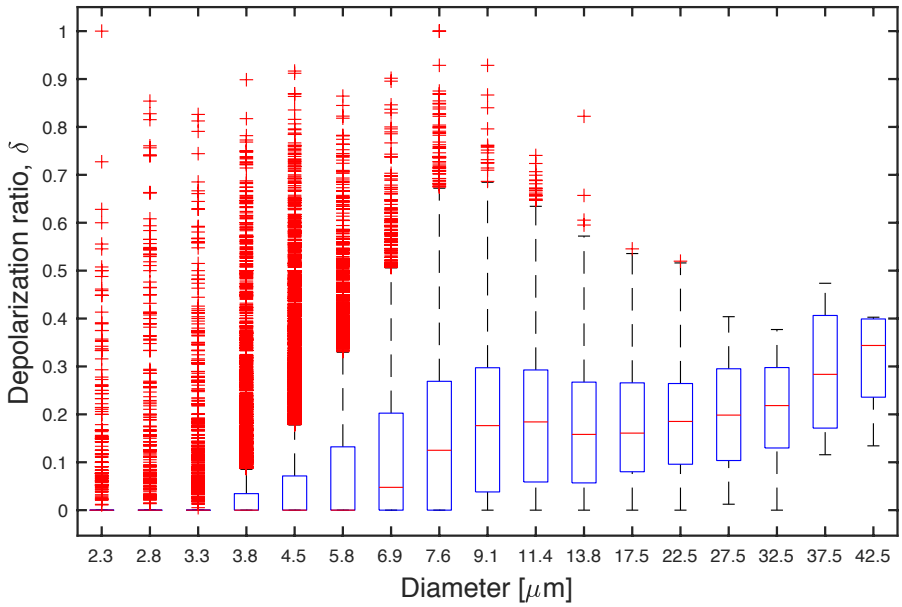

Figure B-1. Box plot of depolarization vs. diameter for CFDC ice crystals for all FIN 02 cases.

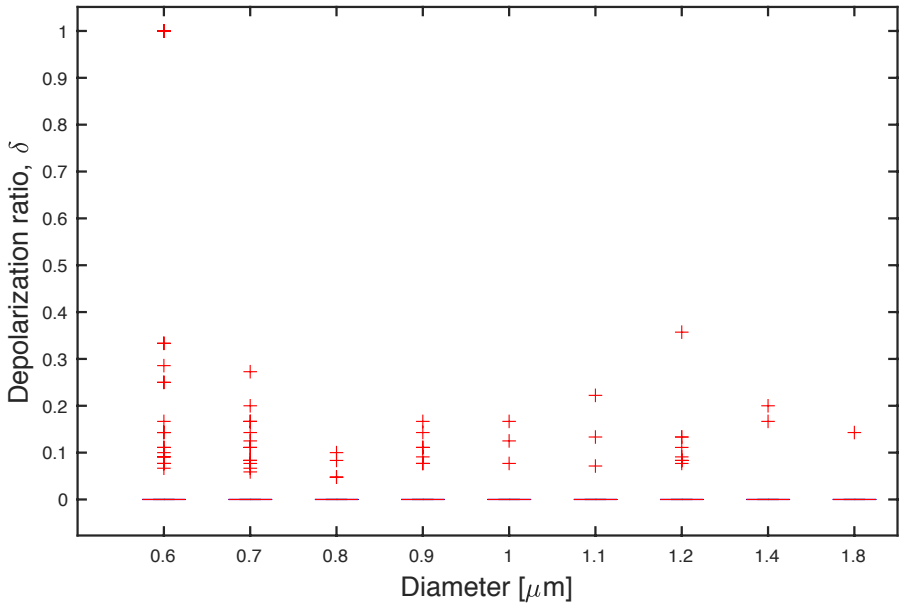

Figure B-2. Box plot of depolarization vs. diameter for CFDC aerosols for all FIN 02 cases.

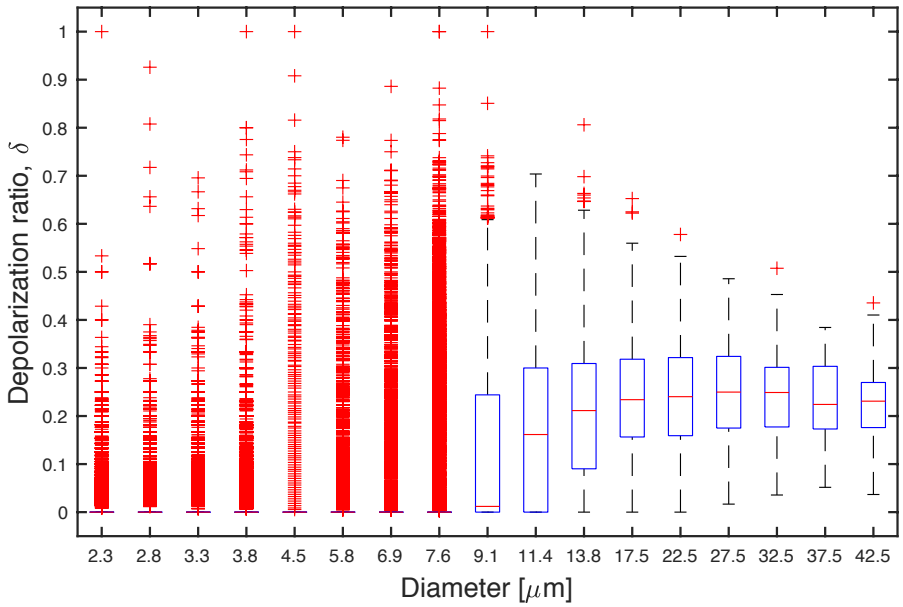

Figure B-3. Box plot of depolarization vs. diameter for CFDC WDBT particles for all FIN 02 cases.